Water Science & Technology

IWA PUBLISHING

Water Science & Technology Vol 84 No 9, 2380 doi: 10.2166/wst.2021.381

Designing of a novel polyvinylidene fluoride/TiO_2/UiO-66-NH_2 membrane with photocatalytic antifouling properties using modified zirconium-based metal-organic framework

Yi-Jing Li[a], Gui-E Chen[a,*], Lian-Jing Liu[a], Zhen-Liang Xu[b], Sun-Jie Xu[b], Huan-Yin Xie[a], Zhen Chen[a] and Jia-Jun Wan[a]

[a] School of Chemical and Environmental Engineering, Shanghai Institute of Technology, 100 Haiquan Road, Shanghai 201418, China
[b] State Key Laboratory of Chemical Engineering, Membrane Science and Engineering R&D Lab, Chemical Engineering Research Center, School of Chemical Engineering, East China University of Science and Technology, 130 Meilong Road, Shanghai 200237, China
*Corresponding author. E-mail: chenguie@sit.edu.cn.

G-EC, 0000-0002-2838-6158; Z-LX, 0000-0002-1436-4927; S-JX, 0000-0002-5973-0871

ABSTRACT

Novel polyvinylidene fluoride/TiO_2/UiO-66-NH_2 (PVDF/TiUN) membranes were produced by the delay phase separation method via introducing the TiO_2/UiO-66-NH_2 (TiUN) nanocomposite into PVDF casting solution. Interconnection of TiO_2 and UiO-66-NH_2 improved photocatalysis capacity and endowed PVDF/TiUN membranes with self-cleaning capability. Quantitative measurements showed that, firstly, PVDF/TiUN membranes exhibited improved photodegradation kinetics and efficiency (up to 88.1%) to Rhodamine B (RhB). Secondly, the performances of bovine serum albumin (BSA) rejection and permeation of PVDF/TiUN membranes outperformed those of other check samples, indicating enhanced hydrophilicity. Thirdly, rejection rate of BSA reached a breathtaking 98.14% and flux recovery ratio (FRR) of BSA reached a breathtaking 95.37%. Thus, given their excellent anti-contamination property and separation performance, the PVDF/TiUN membrane is very likely to be a novel water treatment membrane.

Key words: antifouling property, hydrophilic performance, photocatalytic self-cleaning, polyvinylidene fluoride, Zr-based MOFs

HIGHLIGHTS

- PVDF/TiUN membrane was prepared for the first time via phase separation process method.
- The membrane exhibits excellent antifouling performance with flux recovery ratio of almost 100%.
- PVDF/TiUN membrane showed better removal performance under light conditions.
- Visible light cleaning of fouled membranes enabled high recovery of membrane performance.

GRAPHICAL ABSTRACT

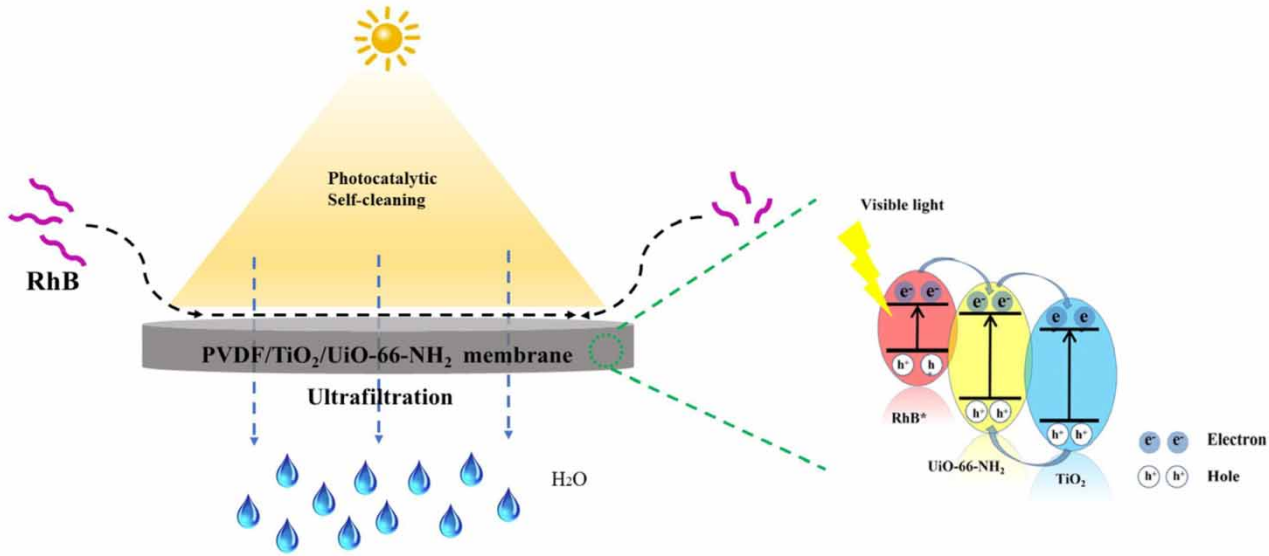

1. INTRODUCTION

Population growth and industrialization lead to the increase of water consumption and exacerbation of water pollution (Shannon *et al.* 2008; Feng *et al.* 2016; Wei *et al.* 2019; Sabri *et al.* 2020). Large amounts of contaminated water produced from industry, agriculture, and households have raised a grave concern. Many techniques have been developed to purify and reuse the wastewater, among which (Gao *et al.* 2014; He *et al.* 2019) membrane-based ultrafiltration (UF) has been recognized as a safe, clean and economical method for separation of extensive contaminants in the wastewater. However, the membrane-based ultrafiltration is also associated with disadvantages, such as fouling effect caused by foulants in the wastewater and large amount of energy and water consumption required for clearing the foulants. Membrane modification by introducing foreign particles with photocatalysis is an efficient method to diminish the fouling effect (Hatat-Fraile *et al.* 2017; Zhang *et al.* 2018; Li *et al.* 2020). Despite the new problem of clogging of the membrane caused by foreign particles, the photocatalytic method remains environmentally and economically friendly for its sustainability in decomposing organic pollutants without generating chemical wastes. In summary, photocatalytic based membrane modification is superior in diminishing membrane fouling effect and improving membrane function (Wang *et al.* 2020).

TiO_2 has been widely used in photocatalytic systems owing to its high hydrophility, excellent light response and suitable energy band location, and highly active photocatalytic performance. However, the wide band gap (3.2 eV) property of TiO_2 made it only reactive to ultraviolet light, limiting its application. Some recent studies have reported the outperformance of MOFs (Metal-Organic Frameworks) materials in adsorption and photocatalysis (Liu *et al.* 2014; Kolesnyk *et al.* 2020; Zhang *et al.* 2020). Among many MOFs, UiO-66 is a newly developed photocatalyst material that can be used for the catalytic degradation of organic pollutants under ultraviolet and visible light. UiO-66-NH_2, a derivative of UiO-66, has large specific surface area, outstanding chemical and thermal stability, and satisfactory charge carrier ability, which made UiO-66-NH_2 a photo-generated charge carrier (Dong *et al.* 2010; Schaate *et al.* 2011; Wang *et al.* 2017; Li *et al.* 2019; Feng *et al.* 2020). In addition, UiO-66-NH_2 has a certain degree of hydrophilicity, which endows the membrane with anti-fouling property. Tran *et al.* (Tran & Chun-Cehieh 2020) designed a PVDF-g-PAA-TGO membrane by grafting TiO_2-GO onto a PVDF membrane and discovered that the membrane exhibited high photocatalytic activity, mainly because of the decreased recombination rate of electron-hole pairs under UV illumination. Kolesnyk *et al.* (2020) synthesized C_3N_4-modified membranes and revealed their anti-fouling property to various types of foulants. Being inspired by those findings, we proposed a complementary strategy – combining MOFs with TiO_2 could facilitate photo-generated electron transfer, enhance the photocatalytic activity and ultimately promote catalytic degradation of organics (Ma *et al.* 2017).

In this study, an ultrafiltration membrane system combining PVDF with TiO_2-modified zirconium-based MOF was established by using the phase inversion technique. The nanoporous MOFs were synthesized and embedded into the membrane (Chen *et al.* 2006; Liu *et al.* 2011; Li *et al.* 2014; Islam *et al.* 2015; Crock *et al.* 2017; Cao *et al.* 2020). Membrane characteristics such as properties of anti-fouling clogging and photocatalytic self-cleaning were measured. The anti-fouling performance of MOF-modified membrane in the purification of protein and dye wastewater was quantified (Venkatesh *et al.* 2016; Wu *et al.* 2016; Shaffer *et al.* 2019; Wang *et al.* 2019).

2. EXPERIMENTAL SECTION

2.1. Materials

Major materials were: PVDF (Solef® 87 6010, Solvay Advanced Polymers); L.L.C (Alpharetta GA, USA); RhB (Sinopharm Chemical Reagent Co.,Ltd); bovine serum albumin (BSA, MW = 58,000, Nanjing Oddfoni Biological Technology Co., Ltd, China). $ZrCl_4$(98%), 2-Aminoterephthalic Acid (98%), Polyvinylpyrrolidone (PVP, K30), HCl (36–38%, AR), TiO_2 (99.8%, AR), N,N-Dimethylacetamide (DMAc, AR), N,N-dimethylformamide (DMF, AR) and Ethanol (AR) were offered by Shanghai Titan Scientific Co., Ltd.

2.2. Synthesis of UiO-66-NH_2 and TiUN

A solvothermal method was used. Typically, 1.0 mmol of $ZrCl_4$ and 1.5 mmol of 2-aminoterephthalic were added into 30 mL of DMF solution. After stirring for 30 min at room temperature, the solution was transferred into a 100 mL Teflon-lined autoclave for solvothermal treatment (353 K for 24 h). After cooling to ambient temperature, the slurry was centrifuged. Precipitates were washed with DMF and absolute ethanol 3 times, before drying (393 K for 12 h in a vacuum oven) to be UiO-66-NH_2 product.

TiUN was synthesized using a similar procedure described above, except replacing pure DMF with TiO_2 suspension.

2.3. Fabrication of membranes

The procedures for preparing PVDF/TiUN membrane are illustrated in Figure 1. For composing the membrane casting solution, PVDF (16 wt.%) and PVP (2 wt.%) were configured at the same percentage and the filler loadings were different. Casting solution constituents were mixed using a blending method, with 5 different combinations described in Table 1. The samples were stirred at 60 °C for 12 h to form a homogeneous solution. The casting solution was immediately casted onto a glass substrate and then immersed in a coagulation bath (deionized water with 0.5 g nanoparticles). The membrane

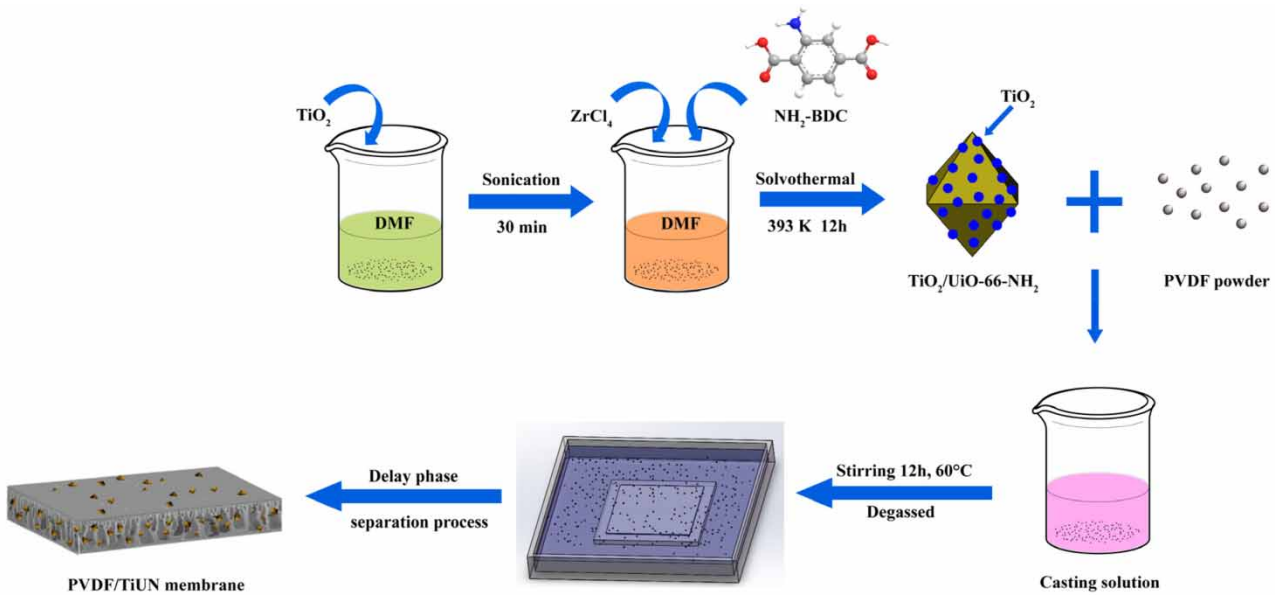

Figure 1 | Illustration of synthetic procedure for PVDF/TiUN membrane.

Table 1 | Compositions of casting solution for MMM membranes

Membranes	PVDF (wt.%)	PVP (wt.%)	DMAC (wt.%)	UiO-66-NH_2 (wt.%)	TiUN (wt.%)
PVDF (M1)	16	2	82	–	–
PVDF/UN0.1 (M2)	16	2	81.9	0.1	–
PVDF/UN0.5 (M3)	16	2	81.5	0.5	–
PVDF/TiUN0.1(M4)	16	2	81.9	–	0.1
PVDF/TiUN0.5(M5)	16	2	81.5	–	0.5

was stored in deionized water after detaching from the glass substrate. To ensure complete phase separation, membranes were immersed into freshwater for around 24 h.

2.4. Characterization of composite materials

Scanning electron microscopy (SEM, S-3400N, Japan), total reflection Fourier infrared spectrometer (FTIR, VERTEX-70, Germany), X-ray diffractometer (XRD, D/max 2200PC, Japan) and X-ray photoelectron spectrometer (XPS, Escalab 250Xi, USA) were used to affirm the topography and composition of nanoparticles.

2.5. Characterization of membranes

FTIR, energy dispersive X-ray spectrometry (EDX) and XPS were used to investigate the chemical components of UF membrane. SEM and atomic force microscopy (AFM, NanoScope IIIa Multimode AFM, USA) were used to characterize membrane structures. Contact anglemeter (XCA-50) was used to measure surface hydrophilicity of membrane (at least 5 repeats) (Ahmad & Hagg 2013). Overall porosity (ε, %) was calculated by Equation (1)

$$\varepsilon = \frac{M_{\mathrm{w}} - M_d}{A \times L \times \rho} \times 100\% \tag{1}$$

In this equation, M_w/M_d denotes wet/dry weights of the membrane; A denotes membrane effective area (m^2); L is the membrane thickness (m) and ρ is water density (0.998 g/cm^3).

Guerout–Elford–Ferry equation (Equation (2)) was used to calculate the mean pore-size (r_m, nm) of the membranes:

$$\mathrm{rm} = \sqrt{\frac{(2.9 - 1.75\varepsilon) \times 8\eta \times L \times Q}{\varepsilon \times A \times \Delta p}} \tag{2}$$

In this equation, η denotes water viscosity (8.9×10^{-4} Pa·s), Q denotes permeated water volume per time unit (m^3/s) and Δp denotes operation pressure (bar).

2.6. Filtration experiments

Prepared membranes were vacuum filtered with pure water (0.1 MPa pressure and 0.333 m^2 effective area). For each membrane, permeated volume was recorded at steady state for 1 h. Permeation flux (J_p) was calculated using Equation (3).

$$J_{\mathrm{p}} = \frac{Q}{A \times \Delta \mathrm{t}} \tag{3}$$

Q denotes permeation volume (L), A denotes membrane area (m^2) and Δt denotes the permeation time (h).

BSA solution was used as the fouling agent (simulated protein solution) to evaluate anti-fouling properties of membranes. At steady state, membrane was infiltrated with distilled water for 30 min and then immediately with BSA solution for 60 min.

Before conducting the second infiltration with distilled water (for 30 min), the fouled membrane was submerged in distilled water for 10 min. Pure-water flux (PWF, kg/m^2.h) and flux recovery ratio (FRR) were obtained using Equation (4):

$$FRR(\%) = \left(\frac{J_c}{J_w}\right) \times 100 \tag{4}$$

J_w and J_c denote membrane PWF before and after BSA filtration. In general, higher FRR indicates better fouling resistance. Different fouling types include total fouling ratio (R_t), reversible fouling ratio (R_r), and irreversible fouling ratio (R_{ir}), calculated as below:

$$R_t(\%) = \left(1 - \frac{J_p}{J_w}\right) \times 100 \tag{5}$$

$$R_r(\%) = \frac{J_c - J_p}{J_w} \times 100 \tag{6}$$

$$R_{ir}(\%) = \left(1 - \frac{J_c}{J_w}\right) \times 100 \tag{7}$$

BSA protein concentration was measured using UV-vis spectroscopy (Shimadzu UV-2450). Membrane rejection value (R) was calculated by Equation (8):

$$R(\%) = \left(1 - \frac{C_P}{C_F}\right) \times 100 \tag{8}$$

C_P and C_F denote BSA concentrations (mg/L) in permeation and feeding solutions respectively.

2.7. Measurement of membrane photo-catalytic function

In the photo-catalytic and adsorption experiment, different types of membrane (3 × 3 cm × 5 pieces for each type) were added to 100 mL RhB solution (10 mg/L, natural pH). For the photocatalytic experiment, membranes were irradiated with visible light in a photocatalytic device (long arc xenon lamp, 500 W; 25 °C; 2 h). The solution was kept in the dark for 30 min to reach adsorption equilibrium before irradiation. The RhB concentration in the feeding and permeation solution was determined by spectrophotometer at 554 nm (UV-vis spectroscopy, HACH, DR6000, USA).

The self-cleaning experiment was conducted in a similar configuration with the antifouling test described above. Each membrane was continuously pressurized for 30 min at 0.1 MPa. After that, RhB solution (300 mg·L^{-1}) was forced to permeate through the membrane at the same operating pressure. In the first round of tests, the fouled membrane was immersed in distilled water (15 min). In the second round of tests, the fouled membrane was placed in water and exposed to ultraviolet light for 15 min to degrade the residual RhB. The self-cleaning property of PVDF/TiUN membrane was evaluated by a separating test of RhB aqueous solution.

3. RESULTS AND DISCUSSION

3.1. Morphologies and phase structures of UiO-66-NH_2 and TiUN

Measurements of functional groups and molecular structures by FTIR spectroscopy are shown in Figure 2(a). The FTIR spectrum measurements of UiO-66-NH_2 revealed the characteristic peaks at ~3444, ~1635, ~1574, ~1434 and ~1384 cm^{-1}, which were corresponded respectively to N-H stretching, C=O stretching vibration, N-H bending vibration, N-H bending vibration and C-N stretching vibration. The characteristic peaks between 600 and 800 cm^{-1} became weaker with the addition of TiO_2, which were attributed to the Zr-O_2 cluster (Islam *et al.* 2017; Ma *et al.* 2017). The FTIR spectrum of TiUN was similar to that of UiO-66-NH_2, indicating that the combination of TiO_2 has limited effect on the intrinsic property of MOFs.

The XRD pattern of the synthesized UiO-66-NH_2 shown in Figure 2(b) was consistent with previous reports, indicating that UiO-66-NH_2 was prepared with high quality. The reflexion angles at ~7.4, ~8.6, ~14.6, ~22.4, ~25.6 correspond to (111), (200), (222), (400), (511) planes, respectively (Starck *et al.* 2012). In addition, the XRD pattern of TiUN and UiO-66-NH_2 matched well, no other distinct diffraction peak was found, indicating that the crystallinity and phase composition of MOF did not change

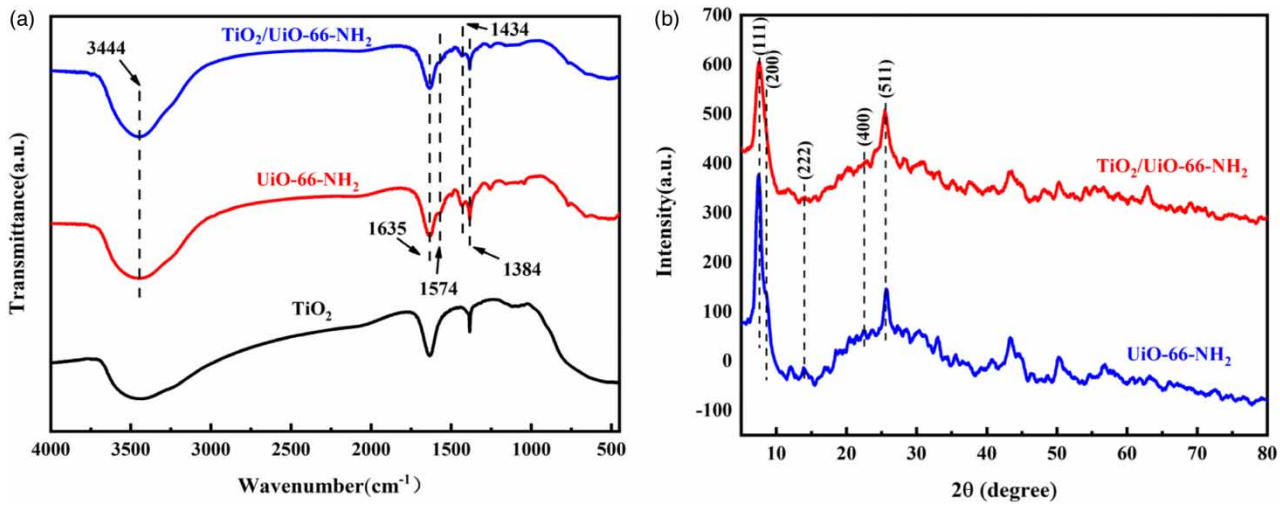

Figure 2 | (a) FTIR spectra of TiO_2, UiO-66-NH_2 and TiUN nanoparticles and (b) XRD patterns of UiO-66-NH_2 and TiUN nanoparticles.

with TiO_2 loading. We found no characteristic peaks for TiO_2, which could be attributed to its low concentration. In general, the result of XRD suggested that structures of UiO-66-NH_2 did not change during the synthesis process (Tambat *et al.* 2018).

As illustrated in Figure 3, the pristine UiO-66-NH_2 exhibited a smooth regular octahedron with particle sizes ranged from 20 to 50 nm. The particle size of nano-TiO_2 was ~5 nm. TiO_2 nanoparticles were dispersed on the surface of UiO-66-NH_2 (Li *et al.*; Zhang *et al.* 2019). We also found that the size of TiUN was uniform, which may be beneficial to acquiring high-performance modified membranes.

3.2. Characterizations of membranes

3.2.1. Chemical composition of membranes

Figure 4(a)–4(c) illustrate the XPS patterns of the PVDF, PVDF/UN and PVDF/TiUN membranes, in which the N 1s and Zr 3d signal the UiO-66-NH_2 in the PVDF/TiUN, which is consistent with a previous report (Li *et al.*; Rajati *et al.* 2019). In comparison with PVDF/UN membrane, PVDF/TiUN membrane showed new signals of Ti 2p. In the modified membranes, a peak signaling O-Ti was observed at 530.08 eV (Liu *et al.* 2018a), which illustrates that TiUN had been mixed with the PVDF membrane successfully.

We further tested the chemical composition of the prepared membranes by FTIR. Functional groups in the PVDF/UN and PVDF/TiUN membranes were analyzed with FTIR spectroscopy. Results are shown in Figure 4(d). In the spectrum band of PVDF membrane, peak 1,406 cm^{-1} attributes to CF_2 and CH_2 deformation vibration. The peaks at 1,070 cm^{-1} and

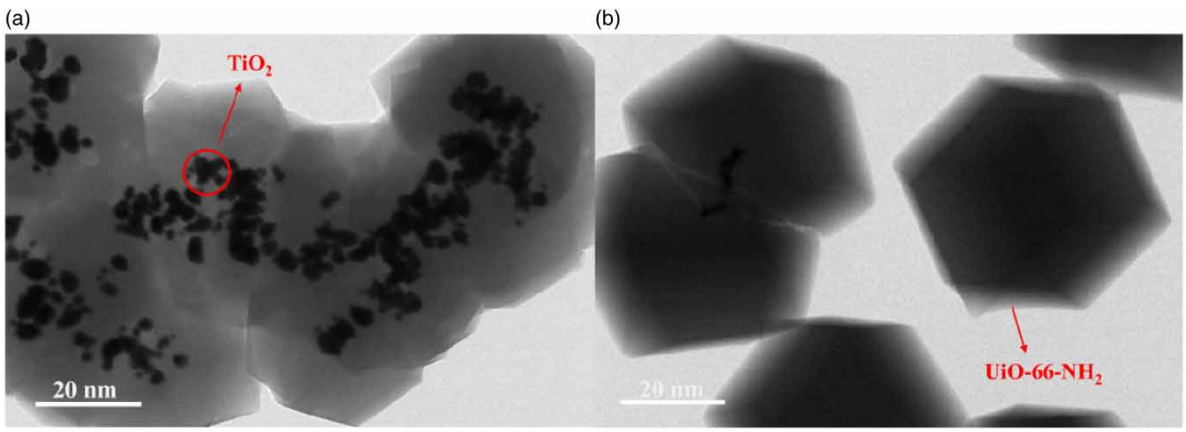

Figure 3 | The transmission electron microscope (TEM) images of (a) TiUN and (b) UiO-66-NH_2.

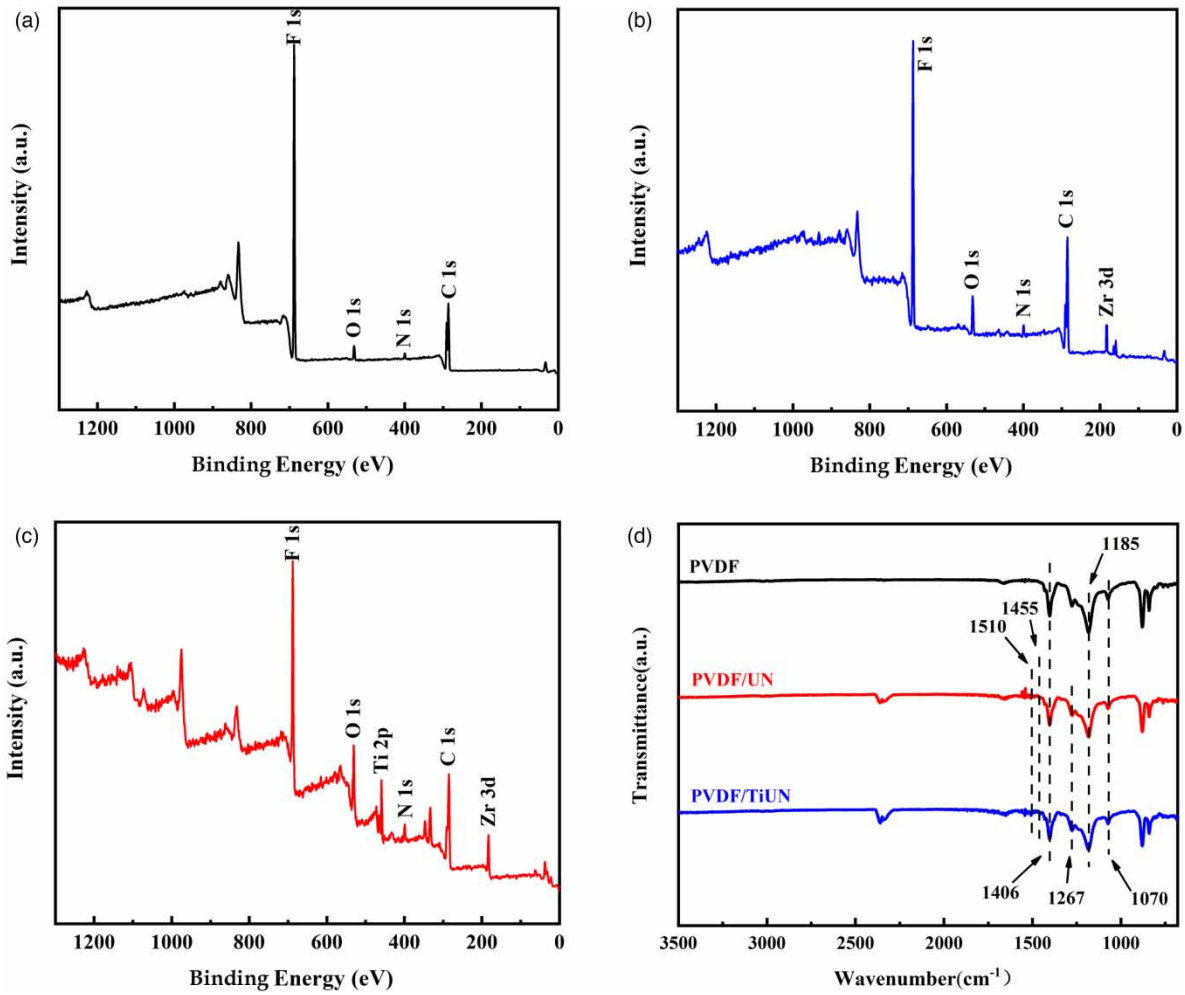

Figure 4 | XPS wide-scan images of (a) M1, (b) M2 and (c) M4; (d) the FTIR spectra of FTIR spectra of M1, M2 and M4.

1,185 cm^{-1} can be attributed to C-C and CF_2 stretching vibration, respectively. Peaks at 400–800 cm^{-1} are attributed to the PVDF characteristic vibration. For the PVDF/UN and PVDF/TiUN membrane, the peak at 1,267 cm^{-1} is the shear stretching of the unique C-N structure in aromatic amine, and the N-H shear stretching vibration in the absorption spectra appears at 1,455 cm^{-1} (Shen *et al.* 2013; Ma *et al.* 2017; Liu *et al.* 2018b).

3.2.2. Membrane morphologies

As shown in Figure 5(a), the cross-sectional images of the membranes showed cavity structures in the sub-layer and asymmetric structures within the dense skin layer. The porosity distribution of the modified membranes (M2, M3, M4 and M5) was more heterogeneous than bare membrane (M1). Moreover, the skin layer in the PVDF/TiUN membrane was thicker than pristine PVDF membrane, which is beneficial to substrate selectivity (Zheng *et al.* 2013). We also noted significant changes in structural texture when the membranes were loaded with different protocol (e.g. M3, M5). This observation could be explained by nanoporous filler not being able to disperse sufficiently in higher loading condition within casting solution. The distribution of nanoparticles in the membranes can be seen in Supplementary Figure 1.

The surface properties of PVDF, PVDF/UN and PVDF/TiUN membranes were measured by AFM. As shown in Figure 5(b), highly rough surfaces provided a foulant trap, thus causing membrane fouling and reducing flux. As summarized in Table 2, the unmodified membrane had a relatively smooth surface with an average roughness of 15.1 nm. Nanoparticle addition decreased surface smoothness of both PVDF/UN and PVDF/TiUN membrane. We found that higher filler loading resulted in a higher roughness of membrane, see M3 & M5 (0.5 wt.%) v.s M2 and M4 (0.1 wt.%), for example. This phenomenon could

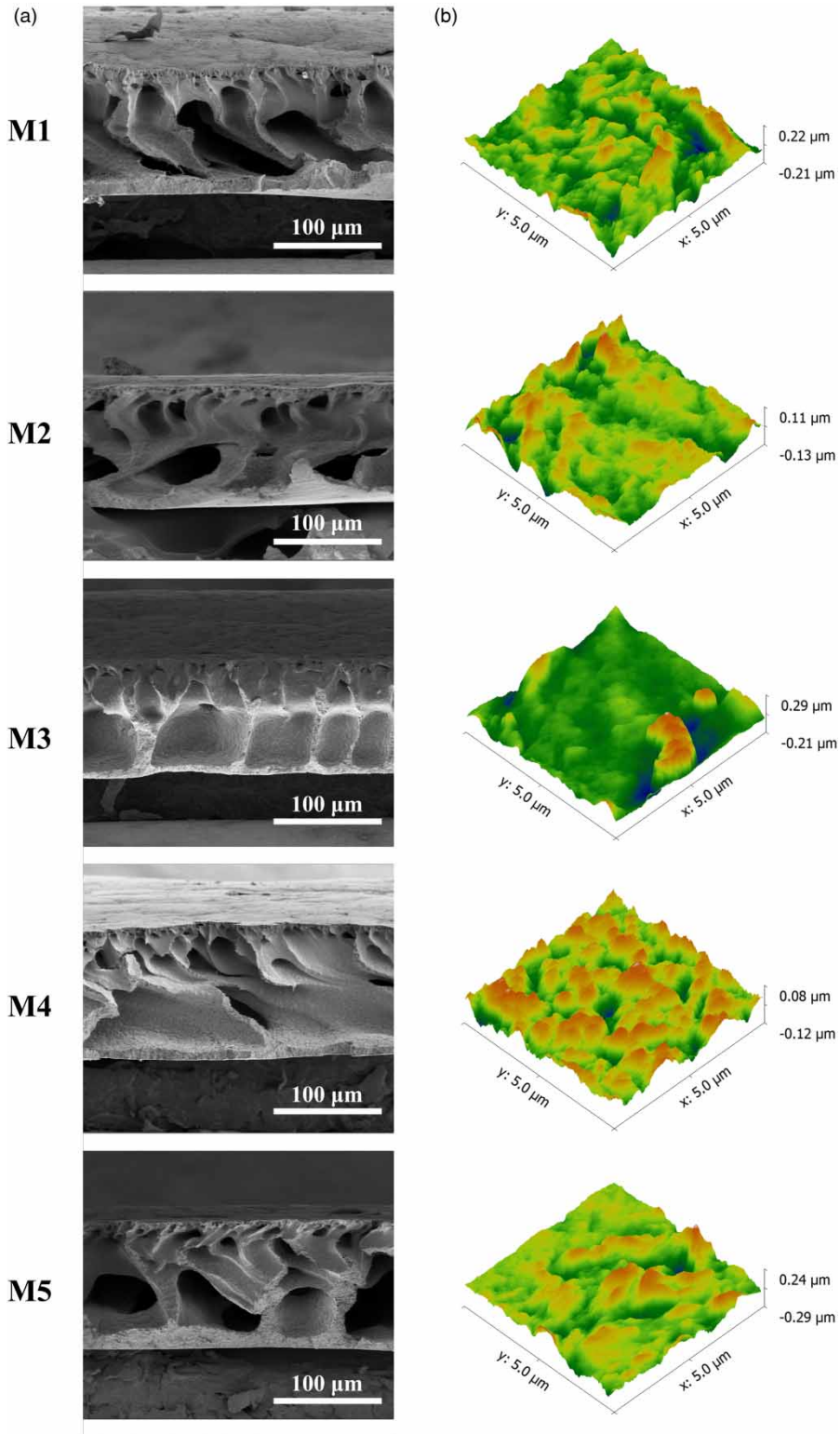

Figure 5 | (a) cross-section SEM images and (b) AFM 3D images of membranes.

be explained by, during phase inversion, MOF particles enriching onto the top layer of the membrane, particularly in higher filler loading condition (Dehghankar *et al.* 2020). The AFM results, FRR and fouling resistance data indicate that M4 (Sa = 9.1 nm) is the optimal membrane that we have configured (Figure 7(c)).

Table 2 | The porosity, mean pore size and roughness of membranes

Membranes	Porosity (%)	Mean pore size (nm)	S_a(nm)	S_q(nm)	S_z(nm)
M1	80.81 ± 1.6	20.06	15.1 ± 0.5	20.3 ± 0.9	73.4 ± 3.2
M2	84.4 ± 1.2	24.39	12.9 ± 0.9	15.8 ± 0.7	60.4 ± 3.6
M3	88.32 ± 2.3	14.6	17.9 ± 0.7	24.1 ± 1.2	87.6 ± 3.7
M4	84.36 ± 0.6	13.49	9.1 ± 1.0	12.6 ± 0.7	55.2 ± 2.8
M5	85.04 ± 1.5	10.85	20.6 ± 0.5	27.9 ± 2.0	96.5 ± 3.5

3.3. Membrane hydrophilicity and water flux

Hydrophilicity is the most important feature of a membrane and is crucial for flux and antifouling properties. We discovered that modified membranes showed higher hydrophilicity in comparison with the bare membrane, as indicated by smaller contact angles (Figure 7).

The high hydrophilicity of the membrane can be explained by two mechanisms. Firstly, the amine groups in MOF strongly attract water molecules through hydrogen bonding. Secondly, MOFs provide a hydration layer that rejects hydrophobic components on the surface of the modified membranes. This hydrophilicity endows the membrane with foulant resistance (antifouling improvement) (Shen *et al.* 2014). As expected, TiO_2 provides extra hydrophilic and endows modified-MOF membrane with smaller contact angles (compared to unmodified-MOF membranes). We noted that the hydrophilicity of modified-MOF membrane was positively correlated with the filler content of the matrix (in a range of 0.1–0.5 wt. %), as indicated by gradual reduction of contact angles.

Figure 7(a) shows the result of PWF measurements of the nanocomposite membranes. We found that the addition of modified-MOF improved membrane hydrophilicity and PWF. Addition of UiO-66-NH_2 (0.1 wt.%) increased PWF, compared with non-addition in the bare membrane (M4 vs. M1). We also noted that PWF decreased with the addition of the unmodified MOF. However, surprisingly, WCA increased as well (Figure 6). This result can be explained by short amine functional group in the MOFs tending to form into cages, because of rich hydrogen bonding. But the cage formation depends on disparity and/or homogeneity, such as agglomeration, of the fillers, which resulted in different flux properties of the MOF-based membrane (modified MOF vs. unmodified MOF) (Li *et al.*). Furthermore, during phase inversion, fillers with smaller size tend to migrate to the surface layer of the membrane, thus forming a dense texture in the top layer and porous texture in the sub layer. This mechanism could also explain the reduction of membrane flux (Bui *et al.* 2021).

3.4. Antifouling performance of the membranes

The fouling behaviors of membranes were examined, and results are shown in Figure 7(b). To evaluate the impact of foulant on the membrane, in the first test we observed that lower additive loading (M2, M4) resulted in a steady reduction trend of foulant effect in the modified membrane, in comparison with the control membrane (M1). The second step was the BSA solution test. Working as a mimetic protein solution, BSA solution exhibited very limited flux for all membranes. In the third step, the recovering test, M4 and M5 possessed the highest PWF.

The dynamic fouling results (flux recovery ratio, FRR) for prepared membranes are summarized in Figure 7(c). As illustrated, membranes containing TiUN had higher FRR, reflecting higher reversible protein adsorption. Basically, this reversibility was attributed to the hydrophilicity of MMMs. Higher surface roughness resulted in depositing of protein molecules irreversibly into surface pores. Higher percentage of TiUN in the membrane caused an increment of surface roughness

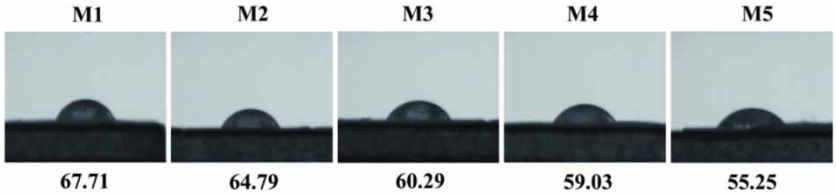

Figure 6 | Demonstrations of water contact angle (WCA) of prepared membranes.

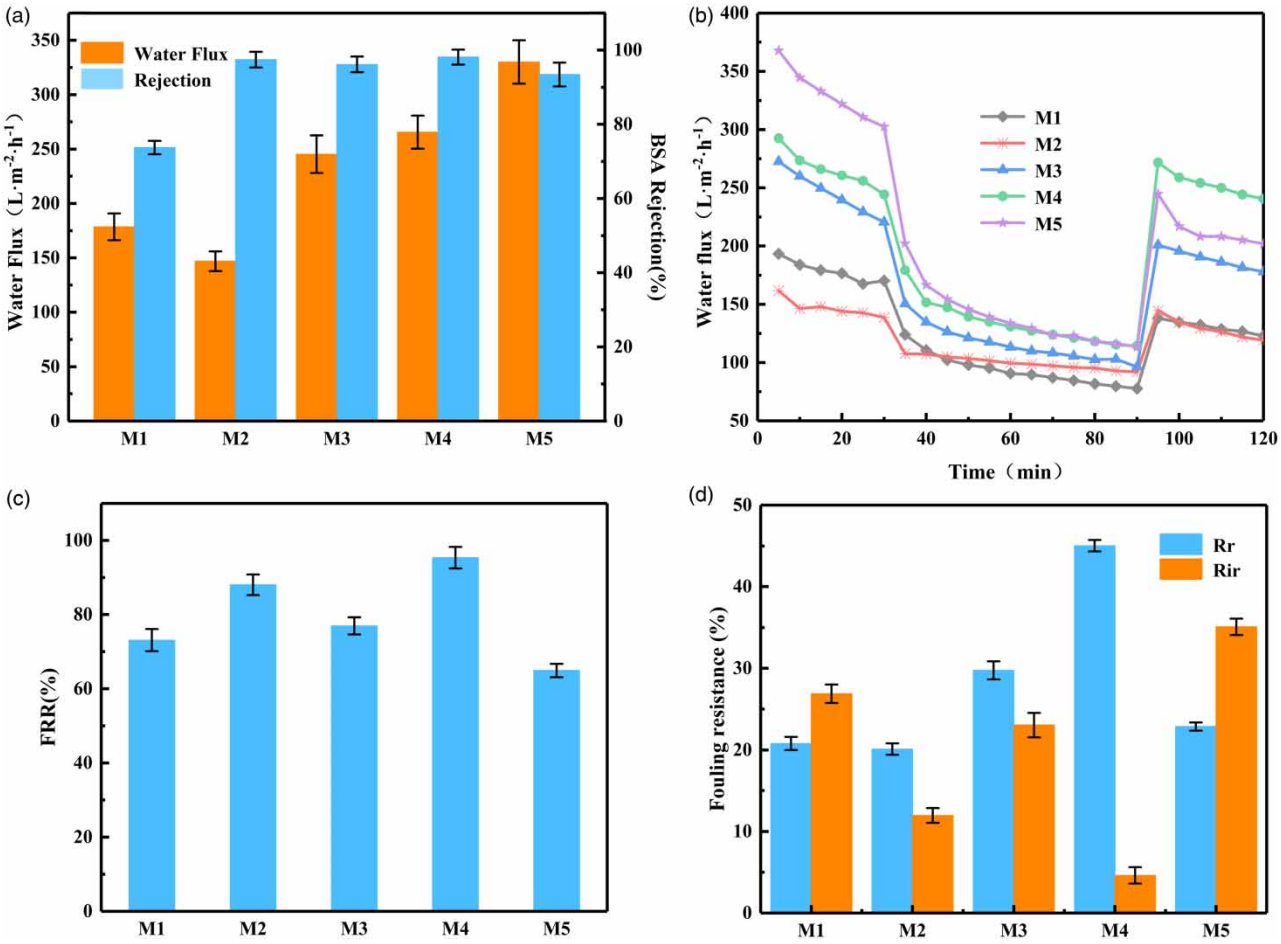

Figure 7 | (a) Pure water flux of membranes with 1 bar trans membrane pressure and removal rate of BSA by all membranes. (b) Fouling behavior for the prepared membranes. (c) Membranes flux recovery ratio after the BSA solution filtration and (d) fouling resistance ratio for the as-prepared ultrafiltration membranes.

and thus lower FRR. M4 (0.1 wt% TiUN) sample showed the highest fouling resistance, which can be attributed to surface roughness and hydrophilicity.

Three parameters, reversible fouling (R_r), irreversible fouling (R_{ir}) and total fouling (R_t) were used to characterize antifouling properties of the membranes. R_r is the fouling part that could be washed out through hydraulic cleaning. R_{ir} is the fouling part that could not be removed with only hydraulic cleaning. R_t reflects the degree of total flux. Values for R_r and R_{ir} were shown in Figure 7(d). Lower R_{ir} value as well as higher FRR indicates better antifouling properties of the membranes. Unfilled PVDF membrane is less hydrophilic and with less surface charge, thus it had a great irreversible fouling ratio (26.88%, exceeding half of 47.67% of total fouling). Among the modified membranes, 0.5 wt.% addition of MOF showed the highest irreversible fouling property. Membrane with addition of 0.1 wt.% PVDF/TiUN had the highest FRR value (95.37%) and the lowest R_{ir} value (4.63%). In summary, surface roughness parameters, R_r, R_{ir} and FRR were improved for MOF modified membranes. Compared with the reported literature, the anti-pollution ability of M4 is higher (Bui *et al.* 2021).

3.5. Photocatalytic performance evaluation of membranes

The RhB degradation and adsorption profiles of M1 membrane, UiO-66-NH_2 membrane and TiUN membrane is shown in Supplementary Figure 2. As illustrated in Supplementary Figure 2a, both TiUN membrane and UN membrane exhibited adsorbability, while bare membrane showed poor adsorbability. This result could be explained by UiO-66-NH_2 providing π-π interaction, electrostatic interaction or hydrogen bonding, which is consistent with a previous study that reported robust ability in RhB separation (Zhang *et al.* 2019). TiUN membrane had good degradation efficiency on RhB while M1

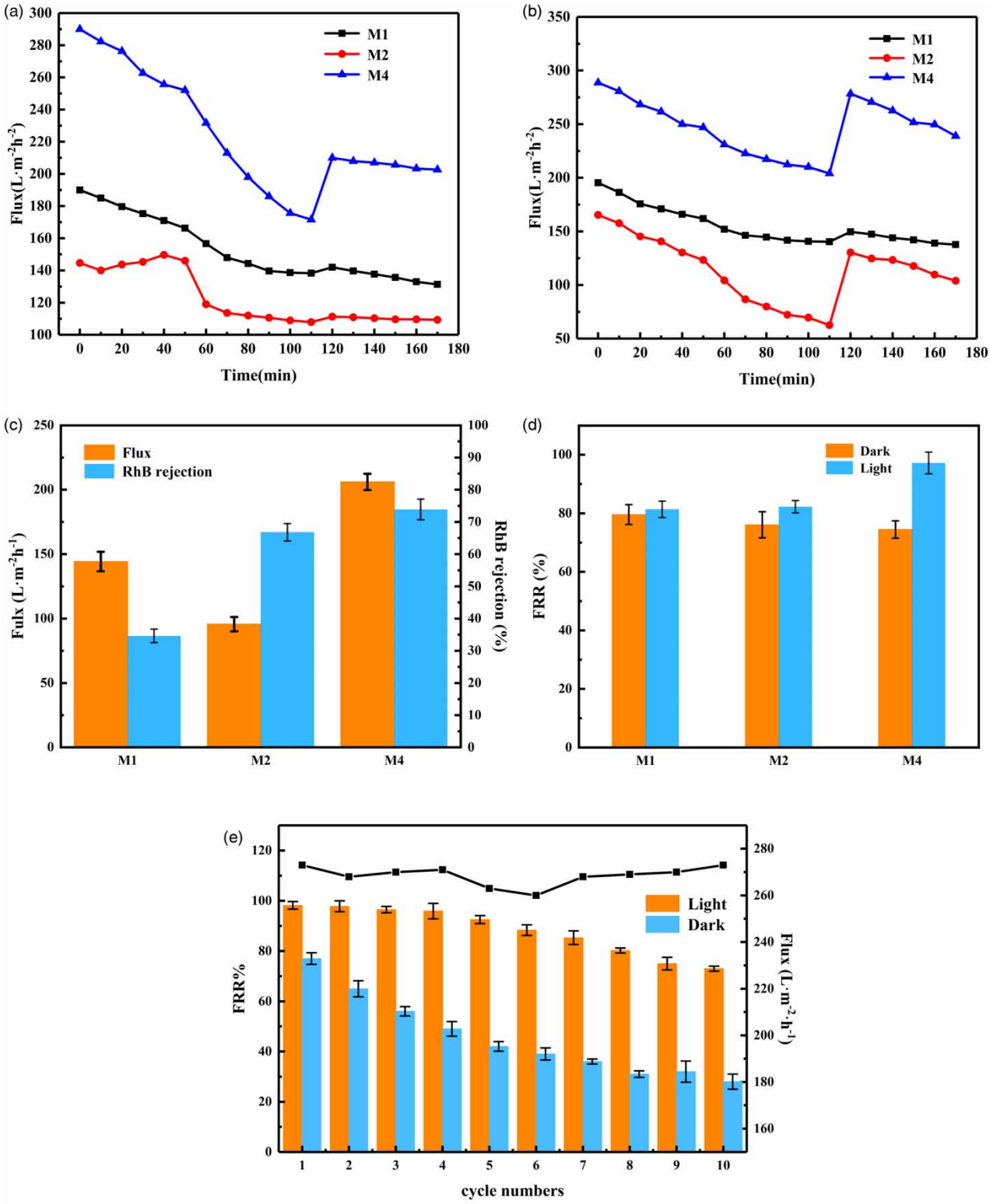

Figure 8 | The time-dependent fluxes of M1, M2 and M4 membranes for water, RhB aqueous solution and water, without visible light exposure (a) or with visible light exposure (b). The removal rate and flux (c) of RhB by three membranes and (d) membrane flux recovery ratio after the BSA solution filtration. (e) The long-term removal effect of M4 membrane on RhB.

membrane had almost no degradation efficiency. This can be attributed to the enhanced absorption of visible light provided by TiO_2 in the membrane. UiO-66-NH_2 has lowest empty molecular orbital and highest occupied molecular orbital, which can transfer electrons and holes and reduce the band gap width of TiO_2, thus expanding the spectral response range. The synergistic effect of TiO_2 and UiO-66-NH_2 enables TiO_2 to generate more photo-generated electrons (PGE) and holes (PGH), promotes the transfer of PGE and inhibits the recombination of PGE and PGH in light condition, resulting in better photocatalytic performance (Li *et al.* 2014; Wu *et al.* 2016; Shaffer *et al.* 2019). These experimental results demonstrated the outperformance of photocatalytic ability of the modified membrane.

3.6. Self-cleaning mechanism

The time-dependent fluxes of M1, M2 and M4 membranes for water and RhB aqueous solution were measured. The result is shown in Figure 8(a) and 8(b). We observed significant drop of flux for all membranes when water was replaced by RhB aqueous solution. This loss of flux is mainly attributed to the deposition or adsorption of RhB on the membrane surface/pores. The flux of all membranes was partly recovered to normal level after hydraulic cleaning. Meanwhile, M4 showed a complete recovery of flux after undergoing photocatalytic self-cleaning process, in contrast to limited recovery of M1 and M2 under the same conditioning. The superior photocatalytic self-cleaning property enables PVDF/TiUN membrane to be promising in water remediation application. The principle of the self-cleaning mechanism is shown in Supplementary Figure 4.

To quantify the separation ability of membranes, we examined the removal effect on RhB of PVDF membrane, PVDF/UN membrane and PVDF/TiUN membrane. As illustrated in Figure 8(c), the removal rate of PVDF/UN membrane and PVDF/TiUN membrane was higher than that of bare membrane. The result could be attributed to the screening and adsorption provided by UiO-66-NH_2 (Yang *et al.* 2019).

The antifouling property on RhB was also examined for bare membrane, PVDF/UN membrane and PVDF/TiUN membrane, under light exposure or dark conditions. As shown in Figure 8(d), in dark conditions, bare membrane showed higher FRR than PVDF/UN membrane and PVDF/TiUN membrane. However, in light exposure conditions, both PVDF/UN membrane and PVDF/TiUN membrane showed higher FRR than bare membrane. Notably, the PVDF/TiUN membrane exhibited an FRR value of 97.2%.

Long-term removal effect of M4 membrane on RhB is shown in Figure 8(e). Under light condition, the FRR% of M4 membrane can reach nearly 100% in the first 3 cycles but decreased to about 85% after the fifth cycle. Under no-light condition, the FRR% of M4 membrane dropped monotonically along all cycles. The flux was almost maintained in light condition while it decreased in the no-light condition (and eventually fell to 50 L m^{-2} h^{-1}). This experiment demonstrated that the PVDF/TiUN membrane exhibited stable flux and FRR% after even 10 cycles of separation, showing its superior recycle ability. In consistents with the recycle ability, the structure of membranes showed substantial stability (Supplementary Figure 3).

4. CONCLUSION AND OUTLOOK

In this report, we adopted a novel method for fabricating TiUN nanohybrid PVDF membranes, which exhibit higher water flux, antifouling, and self-cleaning capacity. The maximum pure water flux of TiUN-0.1 was 265.56 L/(m^2·h), while the BSA rejection rate, WCA and FRR were 98.14%, 59.03°and 95.37% respectively. Furthermore, PVDF/TiUN membrane exhibited superior self-cleaning property as indicated by full recovery of water flux after photocatalytic process. The photocatalytic property, alongside with hydrophilic property endows the TiUN membrane with robust antifouling capacity and superior separation performance. Thus, we offer here a strategy for designing and constructing antifouling membranes with great potential in wastewater remediation, by adopting Zr-based MOFs.

ACKNOWLEDGEMENTS

The authors gratefully acknowledge the financial support received from the National Science and Technology Support Project of China (2014BAB07B01 and 2015BAB09B01) and the Key Technology R&D Program of Shanghai Committee of Science and Technology in China (14231201503).

DATA AVAILABILITY STATEMENT

All relevant data are included in the paper or its Supplementary Information.

REFERENCES

Ahmad, J. & Hagg, M. B. 2013 Preparation and characterization of polyvinyl acetate/ zeolite 4A mixed matrix membrane for gas separation. *J. Membr. Sci.* **427**, 73–84.

Bui, V. T., Abdelrasoul, A. & Mcmartin, D. W. 2021 Investigation on the stability and antifouling properties of polyvinylidene fluoride (PVDF)-zwitterion mixed matrix membranes (MMMs) using molecular dynamics simulation (MDS). *Comput, Mater. Sci.* **187** (5), 110079.

Cao, P., Shi, J., Zhang, J., Wang, X., Jung, J. T., Wang, Z., Cui, Z. & Lee, Y. M. 2020 Piezoelectric PVDF membranes for use in anaerobic membrane bioreactor (AnMBR) and their antifouling performance. *J. Membr. Sci.* **603**, 118037.

Chen, B. L., Liang, C. D., Yang, J., Contreras, D. S., Clancy, Y. L., Lobkovsky, E. B., Yaghi, O. M. & Dai, S. A. 2006 A microporous metal-organic framework for gas-chromato graphic separation of alkanes. *Angew. Chem. Int. Ed* **45**, 1390–1393.

Crock, A., Şengür-Taşdemir, R., Koyuncu, İ. & Tarabara, V. V. 2017 High throughput catalytic dechlorination of TCE by hollow fifiber nanocomposite membranes with embedded Pd and Pd-Au catalysts. *Sep. Purif. Technol.* **179**, 265–273.

Dehghankar, M., Mohammadi, T., Moghadam, M. T. & Tofighy, M. A. 2020 Metal-organic framework/zeolite nanocrystal/poly(vinylidene fluoride) composite ultrafiltration membranes with flux/antifouling advantages. *Mater. Chem. Phys* **260**, 124128.

Dong, H., Ye, P., Zhong, M., Pietrasik, J., Drumright, R. & Matyjaszewski, K. 2010 Superhydrophilic surfaces vis polymer-SiO_2 nanocomposites. *Langmuir* **26**, 15567–15573.

Feng, J., Wang, Q., Fan, D., Ma, L., Jiang, D., Xie, J. & Zhu, J. 2016 Nickel-based xerogel catalysts: synthesis via fast sol-gel method and application in catalytic hydrogenation of p-nitrophenol to paminophenol. *Appl. Surf. Sci.* **382**, 135–143.

Feng, Y. W., Xu, M. J. & Liu, H. 2020 Charge separation and interfacial selectivity induced by synergistic effect of ferroelectricity and piezoelectricity on $PbTiO_3$ monocrystalline nanoplates. *Nano Energy* **73**, 104768.

Gao, Y., Hu, M. & Mi, B. 2014 Membrane surface modification with TiO_2-graphene oxide for enhanced photocatalytic performance. *J. Membr. Sci.* **455**, 349–356.

Hatat-Fraile, M., Liang, R., Arlos, M. J., He, R. X., Peng, P., Servos, M. R. & Zhou, Y. N. 2017 Concurrent photocatalytic and filtration processes using doped TiO_2 coated quartz fiber membranes in a photocatalytic membrane reactor. *Chem. Eng. J.* **330**, 531–540.

He, B., Ding, Y., Wang, J., Yao, Z., Qing, W., Zhang, Y., Liu, F. & Tang, C. Y. 2019 Sustaining fouling resistant membranes: membrane fabrication, characterization and mechanism understanding of demulsification and fouling-resistance. *J. Memb. Sci.* **581**, 105–113.

Islam, M. S., Rahaman, M. S. & Yeum, J. H. 2015 Phosphine-functionalized electrospun poly (vinyl alcohol)/silica nanofibers as highly effective adsorbent for removal of aqueous manganese and nickel ions. *J. Colloid Surf. A: Physicochem. Eng. Asp.* **484** (5), 9–18.

Islam, S., McCutcheon, J. R. & Rahaman, S. 2017 A high flux polyvinyl acetate-coated electrospun nylon 6/SiO_2 composite microfifiltration membrane for the separation of oil-in-water emulsion with improved antifouling performance. *J. Membr. Sci.* **537**, 297–309.

Kolesnyk, I. S., Kujawa, J., Bubela, H. & Konovalova, V. 2020 Photocatalytic properties of PVDF membranes modified with g-C_3N_4 in the process of Rhodamines decomposition. *Sep. Purif. Technol.* **250**, 117231.

Li, X., Fang, X., Pang, R., Li, J., Sun, X., Shen, J., Han, W. & Wang, L. 2014 Self-assembly of TiO_2 nanoparticles around the pores of PES ultrafiltration membrane for mitigating organic fouling. *J. Membr. Sci.* **467**, 226–235.

Li, Y., Ma, C., Nian, P., Liu, H. & Zhang, X. 2019 Green synthesis of ZIF-8 tubular membranes from a recyclable 2- methylimidazole water-solvent solution by ZnO nanorods self-converted strategy for gas separation. *Sep. Purif. Technol.* **581**, 344–354.

Li, R., Li, W. & Jin, C. 2020 Fabrication of ZIF-8@TiO_2 micron composite via hydrothermal method with enhanced absorption and photocatalytic activities in tetracycline degradation. *J. Alloys Compd.* **825**, 154008.

Li, Y., Liu, J.-t., Zhang, K.-h., Lei, L. & Lei, Z.-l. UiO-66-NH_2@PMAA: A hybrid polymer-MOFs architecture for pectinase immobilization. *Pectinase Immobilization* **57** (2), 559–567. doi:10.1021/acs.iecr.7b03398.

Liu, S., Xiang, Z. H., Hu, Z., Zheng, X. P. & Cao, D. P. 2011 Zeolitic imidazolate framework-8 as a luminescent material for the sensing of metal ions and small molecules. *J. Mater. Chem.* **21**, 6649–6653.

Liu, Y., Li, S., Zhang, X., Liu, H., Qiu, J., Li, Y. & Yeung, K. L. 2014 New membrane architecture: ZnO@ZIF-8 mixed matrix membrane exhibiting superb H2 permselectivity and excellent stability. *Inorg. Chem. Commun.* **48**, 77–80.

Liu, N., Huang, W., Zhang, X., Tang, L., Wang, L., Wang, Y. & Wu, M. 2018a Ultrathin graphene oxide encapsulated in uniform MIL-88A(Fe) for enhanced visible light-driven photodegradation of RhB. *Appl. Catal. B Environ.* **221**, 119–128.

Liu, Q., Huang, S., Zhang, Y. & Zhao, S. 2018b Comparing the antifouling effects of activated carbon and TiO_2 in ultrafiltration membrane development. *J. Colloid Interface Sci.* **515**, 109.

Ma, S., Hou, J. J., Yang, H. & Xu, Z. L. 2017 Preparation of renewable porous TiO_2/PVA composite sphere as photocatalyst for methyl orange degradation. *J. Porous Mater.* **25**, 1071–1080.

Rajati, H., Navarchian, A. H., Rodrigue, D. & Tangestaninejad, S. 2019 Improved CO_2 transport properties of Matrimid membranes by adding amine-functionalized PVDF and MIL-101(Cr). *Sep. Purif. Technol.* **235**, 116149.

Sabri, M., Habibi-Yangjeh, A., Chand, H. & Krishnan, V. 2020 Activation of persulfate by novel TiO_2/FeOCl photocatalyst under visible light: facile synthesis and high photocatalytic performance. *Sep. Purif. Technol.* **250**, 117268.

Schaate, A., Roy, P., Godt, A., Lippke, J., Waltz, F., Wiebcke, M. & Behrens, P. 2011 Modulated synthesis of Zr-based metal-organic frameworks: from nano to single crystals. *Chemistry* **17**, 6643–6651.

Shaffer, D. L., Feldman, K. E., Chan, E. P., Stafford, G. R. & Stafford, C. M. 2019 Characterizing salt permeability in polyamide desalination membranes using electrochemical impedance spectroscopy. *J. Membr. Sci.* **583**, 248–257.

Shannon, M. A., Bohn, P. W., Elimelech, M., Georgiadis, J. G., Marinas, B. J. & Mayes, A. M. 2008 Science and technology for water purification in the coming decades. *Nature* **452**, 301–310.

Shen, L., Wu, W., Liang, R., Lin, R. & Wu, L. 2013 Highly dispersed palladium nanoparticles anchored on UiO-66(NH_2) metal-organic framework as a reusable and dual functional visible-light-driven photocatalyst. *Nanoscale* **5**, 9374.

Shen, L., Huang, L., Liang, S., Liang, R., Qin, N. & Wu, L. 2014 Electrostatically derived selfassembly of NH_2-mediated zirconium MOFs with graphene for photocatalytic reduction of Cr(vi). *RSC Adv.* **4**, 2546–2549.

Starck, J., Toppila, E. & Pyykko, I. 2012 Structural determination of a highly stable metal-organic framework with possible application to interim radioactive waste scavenging: Hf-UiO-66. *Phys. Rev. B* **86**, 1514–1517.

Tambat, S. N., Sane, P. K., Srinidhi, S., Nilesh, V. O., Pandit, A. B. & Sontakke, S. M. 2018 Hydrothermal synthesis of NH_2-UiO-66 and its application for adsorptive removal of dye. *Adv. Powder Technol.* **29**, 2626–2632. S0921883118303170-.

Tran, M. L. & Chun-Cehieh, L.-Y. C. 2020 Immobilization of TiO_2 and TiO_2-GO hybrids onto the surface of acrylic acid-grafted polymeric membranes for pollutant removal: analysis of photocatalytic activity. *J. Environ. Chem. Eng.* **8**, 104422.

Venkatesh, K., Arthanareeswaran, G. & Chandra Bose, A. 2016 PVDF mixed matrix nano-filtration membranes integrated with 1D-PANI/TiO_2 NFs for oil–water emulsion separation. *RSC Adv.* **6**, 18899–18908.

Wang, J., Wang, Y., Zhu, J., Zhang, Y., Liu, J. & Van der Bruggen, B. 2017 Construction of TiO_2@graphene oxide incorporated antifouling nanofiltration membrane with elevated filtration performance. *J. Membr. Sci.* **533**, 279–288.

Wang, Y. X., Ma, S., Huang, M. N., Yang, H., Xu, Z. L. & Xu, Z. 2019 Ag NPs coated PVDF@TiO_2 nanofiber membrane prepared by epitaxial growth on TiO_2 inter-layer for 4-NP reduction application. *Sep. Purif. Technol.* **227**, 115700.

Wang, S., Chen, Z., Zhao, Y., Sun, C. & Li, J. 2020 High photocatalytic activity over starfish-like La-doped ZnO/SiO_2 photocatalyst for malachite Green degradation under visible light. *J. Rare Earths.* **234**, 12–34.

Wei, Y., Zhu, Y. & Jiang, Y. 2019 Photocatalytic self-cleaning carbon nitride nanotube in [1] tercalated reduced graphene oxide membranes for enhanced water purification. *Chem. Eng. J.* **356**, 915–925.

Wu, Z. Y., Lin, H. B., Wang, Y. Z., Yu, X. M., Li, J. L., Xiong, Z., Wang, Y., Huang, Y. J., Chen, T. & Liu, F. 2016 Enhanced catalytic degradation of 4-NP using a superhydrophilic PVDF membrane decorated with Au nanoparticles. *RSC Adv* **6**, 62302–62309.

Yang, Z., Zhu, L. & Chen, L. 2019 Selective adsorption and separation of dyes from aqueous solution by core-shell structured NH_2-functionalized UiO-66 magnetic composites. *J. Colloid Interface Sci.* **539**, 76–86.

Zhang, L., Cao, H., Pen, Q., Wu, L., Hou, G., Tang, Y. & Zheng, G. 2018 Embedded CuO nanoparticles@TiO_2-nanotube arrays for photoelectrocatalytic reduction of CO_2 to methanol. *Electrochim. Acta.* **283**, 1507–1513.

Zhang, H., Shi, X. B., Li, J. L., Kumar, P. & Liu, B. 2019 Selective dye adsorption by zeolitic imidazolate framework-8 loaded UiO-66-NH_2. *Nanomaterials* **9**, 18.

Zhang, Y., Zhu, M. & Zhang, S. 2020 Highly efficient removal of U(VI) by the photoreduction of SnO_2/$CdCO_3$/CdS nanocomposite under visible light irradiation. *Appl. Catal. B: Environ.* **279**, 119390.

Zheng, X., Chen, D., Wang, Z., Lei, Y. & Cheng, R. 2013 Nano-TiO_2 membrane adsorption reactor (MAR) for virus removal in drinking water. *Chem. Eng. J.* **230**, 180–187.

First received 28 June 2021; accepted in revised form 31 August 2021. Available online 16 September 2021